

Journal Pre-proofs

Surface pseudocapacitance of mesoporous Mo_3N_2 nanowire anode toward reversible high-rate sodium-ion storage

Yalong Jiang, Jun Dong, Shuangshuang Tan, Qiulong Wei, Fangyu Xiong, Wei Yang, Yuanhao Shen, Qingxun Zhang, Zi'ang Liu, Qinyou An, Liqiang Mai

PII: S2095-4956(20)30499-X
DOI: <https://doi.org/10.1016/j.jechem.2020.07.011>
Reference: JECHEM 1463

To appear in: *Journal of Energy Chemistry*

Received Date: 20 April 2020
Revised Date: 5 July 2020
Accepted Date: 6 July 2020

Please cite this article as: Y. Jiang, J. Dong, S. Tan, Q. Wei, F. Xiong, W. Yang, Y. Shen, Q. Zhang, Z. Liu, Q. An, L. Mai, Surface pseudocapacitance of mesoporous Mo_3N_2 nanowire anode toward reversible high-rate sodium-ion storage, *Journal of Energy Chemistry* (2020), doi: <https://doi.org/10.1016/j.jechem.2020.07.011>

This is a PDF file of an article that has undergone enhancements after acceptance, such as the addition of a cover page and metadata, and formatting for readability, but it is not yet the definitive version of record. This version will undergo additional copyediting, typesetting and review before it is published in its final form, but we are providing this version to give early visibility of the article. Please note that, during the production process, errors may be discovered which could affect the content, and all legal disclaimers that apply to the journal pertain.

© 2020 Published by ELSEVIER B.V. and Science Press on behalf of Science Press and Dalian Institute of Chemical Physics, Chinese Academy of Sciences.



Surface pseudocapacitance of mesoporous Mo₃N₂ nanowire anode toward reversible high-rate sodium-ion storage

Yalong Jiang^{a,1}, Jun Dong^{a,1}, Shuangshuang Tan^a, Qiulong Wei^{b,*}, Fangyu Xiong^a, Wei Yang^a, Yuanhao Shen^a, Qingxun Zhang^a, Zi'ang Liu^a, Qinyou An^a, Liqiang Mai^{a,c,*}

^a *State Key Laboratory of Advanced Technology for Materials Synthesis and Processing, Wuhan University of Technology, Wuhan 430070, Hubei, China*

^b *Department of Materials Science and Engineering, Fujian Key Laboratory of Materials Genome, College of Materials, Xiamen University, Xiamen 361005, Fujian, China*

^c *Foshan Xianhu Laboratory of the Advanced Energy Science and Technology Guangdong Laboratory, Xianhu Hydrogen Valley, Foshan 528200, Guangdong, China*

¹ These authors contributed equally to this work.

*Corresponding authors.

E-mail addresses: qlwei@xmu.edu.cn (Q. Wei); mlq518@whut.edu.cn (L. Mai)

ABSTRACT

Sodium-ion storage devices are highly desirable for large-scale energy storage applications owing to the wide availability of sodium resources and low cost. Transition metal nitrides (TMNs) are promising anode materials for sodium-ion storage, while their detailed reaction mechanism remains unexplored. Herein, we synthesize the mesoporous Mo_3N_2 with nitrogen vacancy in the crystal structure. The sodium-ion storage mechanism of Mo_3N_2 is systematically investigated through *in-situ* XRD, *ex-situ* experimental characterizations and detailed kinetics analysis. Briefly, the Mo_3N_2 undergoes a surface pseudocapacitive redox charge storage process. Benefiting from the rapid surface redox reaction, the mesoporous Mo_3N_2 nanowires (Meso- Mo_3N_2 -NWs) anode delivers high specific capacity (282 mAh g^{-1} at 0.1 A g^{-1}), excellent rate capability (87 mAh g^{-1} at 16 A g^{-1}) and long cycling stability (a capacity retention of 78.6% after 800 cycles at 1 A g^{-1}). The present work highlights that the surface pseudocapacitive sodium-ion storage mechanism enables to overcome the sluggish sodium-ion diffusion process, which opens a new direction to design and synthesize high-rate sodium-ion storage materials.

Keywords: Surface pseudocapacitance; Sodium-ion storage; Nitrogen vacancy; Molybdenum nitride; High-rate

1. Introduction

Electrochemical energy storage (EES) devices, including various types of batteries and electrochemical capacitors, are extensively applied in people's daily lives, including portable electronics, electric vehicles (EVs) and grid storage [1,2]. The mature Li-ion batteries (LIBs) can deliver a high energy density of over 300 Wh kg^{-1} up to now, but their low-rate capability takes hours to recharge. The markets of LIBs are growing very fast, but the lithium resources are limited on earth. Suitable substitutes/supplements to the LIBs are highly desired. The sodium-ion storage devices, including sodium-ion batteries (SIBs) and capacitors (SICs) are regarded as potential alternatives for large-scale energy storage because of the wide availability of sodium resources and low cost [3–7]. However, the ionic radius of Na^+ ($\approx 1.02 \text{ \AA}$) are larger than that of the Li^+ ($\approx 0.76 \text{ \AA}$), usually resulting in slow diffusion kinetics [3]. Thus, the accessible sodium-ion storage mechanism and materials are in urgent demand to reach high-rate capability.

Electrostatic double-layer capacitors (EDLCs) are able to realize the charge or discharge processes in the order of minutes/seconds, however they usually store a limited energy density of $\approx 10 \text{ Wh kg}^{-1}$. Pseudocapacitance [8], battery-like faradaic reactions that occur at capacitor-like high rates, includes redox reactions occurring at surface or near the surface (*e.g.* $\text{RuO}_2 \cdot n\text{H}_2\text{O}$ [9] and VN [10]) and rapid non-diffusion controlled ion intercalation into bulk (*e.g.* $T\text{-Nb}_2\text{O}_5$ [11] and MoS_2 [12]). For decades, many efforts have been devoted to developing suitable pseudocapacitive electrode materials [8]. Transition metal oxides and nitrides had been demonstrated to display pseudocapacitive behavior, whether they are intrinsic materials (such as $T\text{-Nb}_2\text{O}_5$ [11]),

or extrinsic ones (exhibiting surface pseudocapacitance when their crystalline size down to several nanometers, such as V_2O_5 [13] and MoO_3 [14]).

Usually, except from RuO_x , the pseudocapacitive transition metal oxides are poor electronic conductors, hindering their high-rate delivering [15]. Remarkably, TMNs (VN [10,16], TiN [17,18] and NbN [19]) showed the merits of high electrical conductivity, chemical stability and catalytic activity, which have attracted much attention as active materials for pseudocapacitors [20,21]. TMNs have been mostly used as electrodes for aqueous capacitors and delivered excellent rate capability [22,23]. As known, compared with aqueous electrolytes, the non-aqueous systems exhibit wider operation potential window and thus it is able to deliver higher energy density, according to the formula of $E=0.5CV^2$ (where E is the energy density, C is the capacitance and V is the potential range) [9]. Some TMNs have been firstly investigated in non-aqueous lithium-based systems. For example, the Sn_3N_4 delivered a reversible lithium storage capacity of $\approx 1500 \text{ mAh g}^{-1}$ at 0.1 A g^{-1} in $0.001-3 \text{ V}$ (vs. Li^+/Li), which went through a conversion reaction [24]. However, different charge storage performances/behaviors were found in non-aqueous sodium-based systems. The same Sn_3N_4 anode exhibited a much reduced capacity of $\approx 190 \text{ mAh g}^{-1}$ at 0.05 A g^{-1} in 0.001 to 3 V (vs. Na^+/Na) [24]. Comparing their *ex-situ* X-ray diffraction (XRD) patterns under different tested conditions, broad reflections of Sn nanoclusters were observed after delithiation, but the diffraction peaks of Sn_3N_4 remained after desodiation. The above inconsistent behaviors indicated the sodium storage mechanism for Sn_3N_4 might be far different from that for lithium-based system. This kind of different

electrochemical behaviors between lithium and sodium storage were also observed in VN [16], TiN [18] and MoP [25].

Recently, our group proposed a surface redox sodium-ion storage mechanism of transition metal nitrides (*e.g.* TiN [18]) and phosphides (*e.g.* MoP [25]), which explained the insight understandings of the electrochemical behaviors that high-stable closely-packed cubic (or hexagonal) crystal structure delivered the high-rate capability. The surface redox reaction came from their amorphous oxides layers on the nitrides or phosphides nanograins, while inner bulk remained unchanged. Crystal vacancies were used to generate extra host sites for alkalis-ion storage, leading to enhanced electrochemical performance (such as TiO₂ with cation vacancies and MoO_{3-x} with oxygen vacancies) [26–28]. Nitrogen vacancies could be introduced into the TMNs [20]. This raises a question that the TMNs with N-vacancies might affect the sodium-ion storage mechanism and their electrochemical behaviors. However, to the best of our knowledge, there are no works reported on this.

Herein, we successfully synthesized the mesoporous Mo₃N₂ nanowires (Meso-Mo₃N₂-NWs) by controlling the anion exchange process under annealing conditions in ammonia atmosphere. The Mo₃N₂ has a cubic crystal structure with nitrogen vacancy, as shown in Fig. 1(a). The sodium-ion storage behavior and mechanism of the Mo₃N₂ in sodium-based non-aqueous electrolyte were systematically investigated by *in-situ* and *ex-situ* X-ray diffractions (XRD), *ex-situ* transmission electron microscopy (TEM) and detailed kinetics analysis. It was found that the sodium-ion storage mechanism of Mo₃N₂ is surface pseudocapacitive reaction. The delivered capacity is surface-dependent. The Meso-Mo₃N₂-NWs with high specific surface area exhibit remarkable

high-rate and long-term sodium-ion storage performance.

2. Experimental

2.1. Synthesis of Meso-Mo₃N₂-NWs, mesoporous Mo₃N₂ particles (Meso-Mo₃N₂-Ps) and mesoporous MoN nanowires (Meso-MoN-NWs)

The Mo₃O₁₀(C₆H₅NH₃)₂·2H₂O nanowires were prepared through co-precipitation process as reported before [29]. The Mo₃O₁₀(C₆H₅NH₃)₂·2H₂O nanowires were converted to Meso-Mo₃N₂-NWs and Meso-MoN-NWs by annealing in NH₃ flow (70 sccm) at 500 °C for 6 h and 900 °C for 10 h with a heating rate of 5 °C min⁻¹. The commercial MoO₃ powder was converted to Meso-Mo₃N₂-Ps by annealing in NH₃ flow (70 sccm) at 800 °C for 6 h with a heating rate of 5 °C min⁻¹.

2.2. Materials characterization

XRD data were collected by using a D8 Advance X-ray diffractometer with an area detector with Cu *K*α radiation (λ=1.5418 Å) within the range of 10°–80°. The scanning electron microscopy (SEM) and TEM images were observed on JEOL-7100F and Titan G2 60-300 instrument with an image corrector, respectively. X-ray photoelectron spectroscopy (XPS) spectra were recorded using a VG MultiLab 2000 instrument. N₂ adsorption-desorption isotherms were measured by using a Tristar II 3020 instrument at liquid nitrogen temperature (77 K). The electrodes for *ex-situ* characterization were prepared by taking apart the coin cells in an argon-filled glove box. For *ex-situ* XRD tests, the electrode materials were washed with alcohol and dried in glove box. For *ex-situ* TEM experiments, the electrode materials were washed with alcohol and then dispersed in alcohol through ultrasonication.

2.3. Electrochemical measurements

The electrochemical properties were characterized by using 2016-type coin cells with sodium metal foil as the counter electrode. The working electrode was composed of 85 wt% active material, 10 wt% acetylene black and 5 wt% carboxymethyl cellulose (CMC) binder. The slurry was casted on Al foil and dried in a vacuum oven at 120 °C. The active material loading was 1–1.5 mg cm⁻². For *in-situ* XRD tests, the working electrode was obtained using 70% Meso-Mo₃N₂-Ps active material, 20% acetylene black and 10% poly tetrafluoroethylene (PTFE) binder. The electrode slices dried in a vacuum oven at 120 °C. The mass loading of the electrode was 2–2.5 mg cm⁻². The 1 M NaClO₄ in ethylene carbonate/dimethyl carbonate (EC/DMC) (1:1 v/v) + 5% fluoroethylene carbonate (FEC) was used as electrolyte. The cells were assembled in argon-filled glove box. Galvanostatic charge/discharge tests were undertaken on a multi-channel battery testing system (LAND CT2001A) with a cutoff voltage of 0.01–3 V (vs. Na⁺/Na). Electrochemical impedance spectra (EIS) and cyclic voltammetry (CV) were measured on electrochemical workstation (Autolab PGSTAT302N). All measurements were carried out at room temperature.

3. Results and discussion

3.1. Controlled synthesis of Mo₃N₂ materials

Mesoporous nanowires could provide easier electrolyte permeation, shorter ion diffusion distance and faster electron transfer along the axis direction, which are beneficial for obtaining excellent rate and cycling performance [2]. The Mo₃O₁₀(C₆H₈N)₂·2H₂O nanowires (Fig. S1) were used as precursor to synthesize the Meso-Mo₃N₂-NWs and Meso-MoN-NWs [29]. During annealing process,

molybdenum nitrides were obtained through the escape of ammonia and water molecules, importantly, and following anion-exchange process (O^{2-} to N^{3-}) in ammonia atmosphere (Fig. 2(a)). Various annealing temperatures were controlled in the synthesis processes. The powder XRD patterns show that the pure cubic Mo_3N_2 in a $Pm-3m$ space group (JCPDS No. 01-089-3712) was synthesized at 500 °C (Fig. 1(b)), while the pure closely-packed hexagonal-phase MoN in a $P63mc$ space group (JCPDS No. 01-089-5024) was obtained at 900 °C (Fig. S2(a) and (c)). The higher annealing temperature leads to a complete anion exchange process. **Based on the Scherrer Formula, the average size of the Mo_3N_2 nanograins are ≈ 8.7 , 17.2 and 19.9 nm for the Meso- Mo_3N_2 -NWs, Meso- Mo_3N_2 -Ps and Meso-MoN-NWs.** Further, the commercial MoO_3 powders could be changed into Meso- Mo_3N_2 -Ps as the control sample, while a high annealing temperature of 800 °C was needed (Fig. 1(b)).

SEM and TEM were carried out to show the detailed morphology and microstructure. TEM images of Meso- Mo_3N_2 -NWs (Fig. 2(b, c) and Fig. S3), Meso- Mo_3N_2 -Ps (Fig. 2(e) and (f)) and Meso-MoN-NWs (Fig. S2(b)) show that the samples consist of interconnected nanograins and inner pores. The creating of pores is owing to the escape of ammonia and water molecules and then strain releases by large lattice mismatch during the anion-exchange process [30,31]. The high-resolution TEM (HRTEM) images of Meso- Mo_3N_2 -NWs (Fig. 2(d)) and Meso- Mo_3N_2 -Ps (Fig. 2(g)) reveal lattice fringes with d -spacing of about 0.21 and 0.25 nm, corresponding to the (200) and (111) planes of Mo_3N_2 with cubic structure (space group: $Pm-3m$). The selected area electron diffraction (SAED) patterns further confirm the crystallization nature of the Meso- Mo_3N_2 -NWs (inset of Fig. 2(d)) and Meso- Mo_3N_2 -Ps (inset of Fig. 2(g)). Interestingly, the nanograins in Meso- Mo_3N_2 -NWs are almost iso-oriented and

the [100] preferred orientation along the axial direction of nanowires has been demonstrated by the HRTEM image and SAED pattern (Fig. 2(d) and inset of Fig. 2(d)), resulting in the higher electronic transport [32]. The high-angle annular dark-field (HAADF) images and the corresponding elemental mappings of Meso-Mo₃N₂-NWs and Meso-Mo₃N₂-Ps show the existence of Mo, N and O (Fig. S4).

Nitrogen adsorption-desorption isotherms were further measured to characterize the mesoporous structure of the samples (Fig. 2(h) and Fig. S2(d)). The Brurauer-Emmerr-Teller (BET) surface areas of Meso-Mo₃N₂-NWs, Meso-Mo₃N₂-Ps and Meso-MoN-NWs are 55.2, 7.6 and 3.4 m² g⁻¹, respectively (Table S1). It is worth noting that the nitrogen adsorption-desorption isotherms of Meso-Mo₃N₂-NWs is a type-IV curve with an B hysteresis loop, which is related to slit-like mesoporous [33], consistent with the TEM observation (Fig. 2(c)). The Barrett-Joyner-Halenda (BJH) pore-size distribution curves show a narrow pore size of ≈4 nm for Meso-Mo₃N₂-NWs, while that is 4~18 and 20~65 nm for Meso-Mo₃N₂-Ps and Meso-MoN-NWs, respectively (Fig. S2(e) and Fig. S5). With the increasing temperature, the hollow space and BET surface areas of the as-obtained samples become much smaller owing to that the higher temperature accelerates the exchange rates of N³⁻ with O²⁻ anions and nanograins grow up and merge together [34]. XPS was measured to characterize the surface chemistry compositions of the products. After peak fitting, Mo 3d peaks of the samples exhibit complex signals that comprise the doublets of several oxidation states (Fig. 2(i) and Fig. S2(f)). Two peaks located at 229.2 and 232.0 eV are attributed to formation of Mo-N bond. The other two doublets at 229.9/232.6 eV (Mo 3d_{5/2}/3d_{3/2}) and 233.6/235.8 eV (Mo 3d_{5/2}/3d_{3/2}) are assigned to high oxidation state of Mo (Mo⁴⁺ and Mo⁶⁺) owing to the fact that the formation of oxides layer at the nanograins' surface when exposed in air [35–37]. Further, based on the ratios between the fitting areas of different Mo

valance state (Table S2), the content of surface MoO_x (Mo^{6+} and Mo^{4+}) of Meso- Mo_3N_2 -NWs (60.1%) is about same as that of Meso- Mo_3N_2 -Ps (57.3%) and Meso-MoN-NWs (50.7%).

3.2. Sodium-ion storage performance of Mo_3N_2

The electrochemical performance of the Mo_3N_2 was investigated by assembling the coin cells (2016-type) with metallic sodium as the counter and reference electrode. Fig. 3(a) shows the CV curves of Meso- Mo_3N_2 -NWs electrodes, measured in 0.01–3 V (vs. Na^+/Na) at a scan rate of 0.2 mV s^{-1} . At the first discharge cycle, a well-defined peak located at $\approx 1 \text{ V}$ is possibly attributed to the formation of a solid electrolyte interphase (SEI) layer [18,38]. The galvanostatic charge-discharge curves of Meso- Mo_3N_2 -NWs, Meso- Mo_3N_2 -Ps and Meso-MoN-NWs exhibit the slope line-like voltage response at a specific current of 0.1 A g^{-1} (Fig. 3(b) and Fig. S6(a)) and the first coulombic efficiency of Meso- Mo_3N_2 -NWs is 80.4%. Rate capabilities for the samples were shown in Fig. 3(c) and Fig. S6(b). Remarkably, Meso- Mo_3N_2 -NWs deliver a capacity of 87 mAh g^{-1} at the specific current up to 16 A g^{-1} . The linear-like galvanostatic charge-discharge curves of Meso- Mo_3N_2 -NWs at different rates remain well, indicating a capacitive charge storage behavior (Fig. 3(d)). When the rate returns to 0.5 A g^{-1} , capacity could reversibly recover to about 229 mAh g^{-1} . The Meso- Mo_3N_2 -NWs also display excellent long-term cycling performance at 1 A g^{-1} , as shown in Fig. 3(e). Compared to the Meso- Mo_3N_2 -Ps and Meso-MoN-NWs (Fig. S6(c)), the Meso- Mo_3N_2 -NWs deliver a high reversible specific capacity of 272 mAh g^{-1} , and a high capacity retention of 78.6% after 800 cycles is achieved. Fig. 3(f) displays the similar

galvanostatic charge-discharge curves at different cycles, indicating a highly reversible charge storage process. To sum up, the rate capability of previous reported sodium-ion storage anode materials are shown in Fig. 3(g) and Table S3. The Meso-Mo₃N₂-NWs in this work display superior rate capability when compared to those of hard carbon [39], TiO₂ [40], expanded graphite [41], MoS₂-C [42], Na₂Ti₃O₇ [43] and MXenes Ti₂CT_x [44].

3.3. Sodium-ion storage mechanism of Mo₃N₂

The high crystalline Meso-Mo₃N₂-Ps was first investigated by XRD measurements at various (de)sodiation states to further check the phase changes during the discharge and charge processes. The *in-situ* XRD patterns (Fig. 4(a)) and *ex-situ* XRD patterns (Fig. S7) of Meso-Mo₃N₂-Ps both display the unchanged diffraction peaks of Mo₃N₂ during sodiation and desodiation, indicating a non-phase change process. The similar results were also detected on Meso-Mo₃N₂-NWs by *ex-situ* XRD tests (Fig. 4(c)). *Ex-situ* TEM measurement was undertaken to confirm these phenomena as well. Based on the corresponding SAED patterns of sodiated Meso-Mo₃N₂-Ps (inset of Fig. 4(b)), the crystalline of Mo₃N₂ remains, which is consistent with the *in-situ* and *ex-situ* XRD results. The mesoporous structure of Meso-Mo₃N₂-Ps is retained after the first sodiation process (Fig. 4(b)). The *ex-situ* TEM images of Meso-Mo₃N₂-NWs when discharged to 0.01 V (Fig. 4(d)) at first cycle and after 500 cycles (Fig. S8) were collected. The mesoporous nanowires are maintained well when discharged to 0.01 V, indicating robust structural stability during the sodiation process. The corresponding SAED pattern shows the diffraction spots corresponded to (200) and (111) planes of Mo₃N₂

(inset of Fig. 4(d)), revealing the remain of crystallization nature of the Meso-Mo₃N₂-NWs after sodiation. Noticeably, the crystal structure of Mo₃N₂ keeps the same based on the diffraction rings even after 500 cycles (inset of Fig. S8). The corresponding EDS mappings demonstrate the distribution of Mo, N, O and Na elements (Fig. S9(a) and (b)). EIS was measured to provide further insights. Fig. S10 displays the Nyquist plots for Meso-Mo₃N₂-NWs after different cycles, which are made up of a depressed semicircle (feature of charge transfer resistance, R_{ct}) in the medium-frequency region and an oblique line (feature of ion diffusion resistance) in the low-frequency region [45]. The diameter of the depressed semicircle decreases sharply after activation, which is conducive to the capacity retention at high rates. Meanwhile, the retention of R_{ct} even after 100 cycles suggests a formation of stable SEI films during cycles, which is beneficial for long-cyclic stability.

CV curves of Meso-Mo₃N₂-NWs (Fig. 5(a) and Fig. S11(a)) and Meso-Mo₃N₂-Ps (Fig. 5(b) and Fig. S11(b)) at scan rates ranging from 0.2 to 10 mV s⁻¹ were characterized to analyze the diffusion kinetics process. A distinct pair of redox peaks located at about 0.3 and 0.6 V are observed, corresponding to the faradaic redox reaction of surface molybdenum oxides [46]. The currents of redox peaks enhance while the locations shift slightly as the scan rate increases, indicating excellent rate performance. A quantification analysis is taken to investigate the relationship between the peak current (i) and scan rate (ν) bases on the Eq. (1) [9,47]:

$$i = a\nu^b \quad (1)$$

The parameter b is determined by plotting $\log(i)$ versus $\log(\nu)$. When $b=0.5$, the peak

current is proportional to the square root of the sweep rate, indicating a semi-infinite diffusion-controlled charge storage, whereas $b=1$ represents a capacitance-dominated process. As displayed in Fig. 5(c), the b -values of Meso-Mo₃N₂-NWs and Meso-Mo₃N₂-Ps are 0.95 and 0.90, which are close to 1, indicating capacitance-dominated charge storage. Further, the diffusion-controlled and capacitive contributions to total capacity at a fixed potential (V) were analyzed according to the Eq. (2) [9,47]:

$$i(V) = k_1v + k_2v^{1/2} \quad (2)$$

Fig. 5(d) and Fig. S11(c) display CV curves of Meso-Mo₃N₂-NWs and Meso-Mo₃N₂-Ps at 1 mV s⁻¹ with shaded portions for the capacitive contributions, respectively. The capacitive contributions of Meso-Mo₃N₂-NWs (86%) and Meso-Mo₃N₂-Ps (66%) are obtained at the sweep rate of 1 mV s⁻¹, indicating a relatively high capacitive response in the charge storage process. Usually, EDLC mainly depended on the specific surface area (SSA). Taking the consideration of areal capacitance of 10–20 μF cm⁻² for EDLC [48] and the surface area of 55.2 m² g⁻¹ for Meso-Mo₃N₂-NWs, the capacity from EDLC is ≈25 mAh g⁻¹, which is ≈0.09% of the delivered capacity. Thus, the charge storage of Mo₃N₂ is a capacitance-dominated process.

According to previously reported sodium-ion storage mechanisms, intercalation-type materials (such as Na₂Ti₃O₇ [43], MXene-Ti₂CT_x [44], and NaTi₂(PO₄)₃ [49]) underwent single-phase (solid-solution) or two-phase reactions, corresponding to the shift of XRD peaks under (de)sodiation. For conversion-type materials (such as NiCo₂O₄ [50], CoS_x [51], Cu₂Se [52] and Sb₂O₄ [53]), they underwent a dramatic amorphization process at the first cycle accompanied with the disappearance of XRD

peaks. Herein, the crystal sizes of Meso-Mo₃N₂-NWs and Meso-Mo₃N₂-Ps are very small of ≈ 8.7 and 17.2 nm, which is very short ion diffusion distances. However, the Meso-Mo₃N₂-NWs delivered a capacity of 282 mAh g⁻¹, much higher than that of 109 mAh g⁻¹ for Meso-Mo₃N₂-Ps. As confirmed by above *in-situ* and *ex-situ* XRD patterns, and *ex-situ* TEM observations (Fig. 4 and Fig. S7), there are no shifts of the XRD peaks and the Mo₃N₂ crystal structure remains the same during the (de)sodiation processes. This was very different from the normal intercalation or conversion reaction [5–7], which confirmed that the Mo₃N₂ with the N-vacancies did not provide the host sites for sodium-ion intercalation. The possible explanation is that the delivered capacity comes from the faradaic redox reaction of surface molybdenum oxides on Mo₃N₂ nanograins, while there are no changes in the bulk Mo₃N₂ phase. According to the XPS data, the surface MoO_x content of Meso-Mo₃N₂-NWs (60.1%) and Meso-Mo₃N₂-Ps (57.3%) is close. **Considering that XPS test is a near-surface characterization technology, the weight percentages of surface MoO_x would increase when the inner Mo₃N₂ has much smaller nanograin size and higher surface area.** The specific surface areas of Meso-Mo₃N₂-NWs (55.2 m² g⁻¹) is much larger than that of Meso-Mo₃N₂-Ps (7.6 m² g⁻¹), thus leading to the enhanced specific capacity. Fig. 4(e) schematically displays the surface pseudocapacitive sodium storage mechanism. The surface molybdenum oxides on Mo₃N₂ undergo a pseudocapacitive surface redox reaction while the inner Mo₃N₂ is unreactive during sodiation/desodiation processes.

4. Conclusions

In summary, Mo₃N₂ with nitrogen vacancy in cubic crystal structure are

successfully synthesized and investigated as the sodium-ion storage anode material for the first time. We deeply study the sodium-ion storage behavior and mechanism of Mo_3N_2 anode. Based on systematical *in-situ* and *ex-situ* XRD and TEM characterizations, it is proved that the sodium-ion storage mechanism of Mo_3N_2 is a surface redox reaction, that is the surface molybdenum oxides on Mo_3N_2 undergo a faradaic redox reaction while inner Mo_3N_2 is unchanged. Besides, the surface redox reaction is a capacitance-dominated charge storage process, which enables the high-rate capabilities. As a result, Meso- Mo_3N_2 -NWs with large surface area deliver excellent rate performance (282 mAh g^{-1} at 0.1 A g^{-1} and 87 mAh g^{-1} at 16 A g^{-1}) and a long cyclic retention of 78.6% at 1 A g^{-1} after 800 cycles. The surface pseudocapacitance-dominated active materials with masterly nanostructural constructing are able to deliver comparable specific capacity than those of intercalation-type materials (Fig. 3(g)), but importantly the former display better high-rate capability. Considering the present Mo_3N_2 , MoN and previously reported TiN [18] and MoP [25], the surface redox sodium-ion storage mechanism is different from typically intercalation or conversion reactions. The deep understanding of surface pseudocapacitive sodium-ion characteristic provides an effective strategy to design and synthesize active materials for high-rate sodium-ion storage devices.

Declaration of competing interest

The authors declare that they have no known competing financial interests or personal relationships that could have appeared to influence the work reported in this

paper.

Acknowledgments

This work was supported by the National Natural Science Foundation of China (51832004, 51521001), the National Key Research and Development Program of China (2016YFA0202603), the Program of Introducing Talents of Discipline to Universities (B17034), the Yellow Crane Talent (Science & Technology) Program of Wuhan City, Foshan Xianhu Laboratory of the Advanced Energy Science and Technology Guangdong Laboratory (XHT2020-003), and the “Double-First Class” Foundation of Materials and Intelligent Manufacturing Discipline of Xiamen University.

Appendix A. Supplementary data

Supplementary data to this article can be found online at xxx

References

- [1] B. Dunn, H. kamath, J.M. Tarascon, *Science* 334 (2011) 928-935.
- [2] Q. Wei, F. Xiong, S. Tan, L. Huang, E. H. Lan, B. Dunn, L. Mai, *Adv. Mater.* 29 (2017) 1602300.
- [3] N. Yabuuchi, K. Kubota, M. Dahbi, S. Komaba, *Chem. Rev.* 114 (2014) 11636-11682.
- [4] C. Vaalma, D. Buchholz, M. Weil, S. Passerini, *Nat. Rev. Mater.* 3 (2018) 18013.
- [5] L. Li, Y. Zheng, S. Zhang, J. Yang, Z. Shao, Z. Guo, *Energy Environ. Sci.* 11 (2018) 2310-2340.
- [6] Y. Liang, W.H. Lai, Z. Miao, S.L. Chou, *Small* 14 (2018) 1702514.
- [7] T. Wang, D. Su, D. Shanmukaraj, T. Rojo, M. Armand, G. Wang, *Electro. Ener. Rev.* 1 (2018) 200-237.
- [8] C. Choi, D.S. Ashby, D.M. Butts, R.H. DeBlock, Q. Wei, J. Lau, B. Dunn, *Nat. Rev. Mater.* (2019), 1-15.
- [9] V. Augustyn, P. Simon, B. Dunn, *Energy Environ. Sci.* 7 (2014) 1597-1614.
- [10] D. Choi, G.E. Blomgren, P.N. Kumta, *Adv. Mater.* 18 (2006) 1178-1182.
- [11] J.W. Kim, V. Augustyn, B. Dunn, *Adv. Energy Mater.* 2 (2012) 141-148.
- [12] J.B. Cook, H.S. Kim, T.C. Lin, C.H. Lai, B. Dunn, S.H. Tolbert, *Adv. Energy Mater.* 7 (2017) 1601283.
- [13] Z. Chen, V. Augustyn, X. Jia, Q. Xiao, B. Dunn, Y. Lu, *ACS Nano* 6 (2012) 4319-4327.

- [14] T. Brezesinski, J. Wang, S.H. Tolbert, B. Dunn, *Nat. Mater.* 9 (2010) 146.
- [15] Q. Wang, M. Shang, Y. Zhang, Y. Yang, Y. Wang, *ACS Appl. Mater. Interfaces* 10 (2018) 7162-7170.
- [16] L. Wang, J. Sun, R. Song, S. Yang, H. Song, *Adv. Energy Mater.* 6 (2016) 1502067.
- [17] S. Dong, X. Chen, L. Gu, X. Zhou, H. Wang, Z. Liu, P. Han, J. Yao, L. Wang, G. Cui, *Mater. Res. Bull.* 46 (2011) 835-839.
- [18] J. Dong, Y. Jiang, Q. Li, Q. Wei, W. Yang, S. Tan, X. Xu, Q. An, L. Mai, *J. Mater. Chem. A* 5 (2017) 10827-10835.
- [19] D. Choi, P.N. Kumta, *J. Am. Chem. Soc.* 94 (2011) 2371-2378.
- [20] Y. Zhong, X. Xia, F. Shi, J. Zhan, J. Tu, H.J. Fan, *Adv. Sci.* 3 (2016) 1500286.
- [21] M.S. Balogun, W. Qiu, W. Wang, P. Fang, X. Lu, Y. Tong, *J. Mater. Chem. A* 3 (2015) 1364-1387.
- [22] P. Pande, A. Deb, A.E. Sleightholme, A. Djire, P.G. Rasmussen, J. Penner-Hahn, L.T. Thompson, *J. Power Sources* 289 (2015) 154-159.
- [23] A. Djire, J.B. Siegel, O. Ajenifujah, L. He, L.T. Thompson, *Nano Energy* 51 (2018) 122-127.
- [24] X. Li, A.L. Hector, J.R. Owen, S.I.U. Shah, *J. Mater. Chem. A* 4 (2016) 5081-5087.
- [25] Y. Jiang, Y. Shen, J. Dong, S. Tan, Q. Wei, F. Xiong, Q. Li, X. Liao, Z. Liu, Q. An, L. Mai, *Adv. Energy Mater.* 9 (2019) 1900967.
- [26] C. Chen, P. Li, T. Wang, S. Wang, M. Zhang, *Small* 15 (2019) 1902201.
- [27] H.S. Kim, J.B. Cook, H. Lin, Jesse S. Ko, Sarah H. Tolbert, V. Ozolins, B. Dunn, *Nat. Mater.* 16 (2017) 454-460.
- [28] T. Koketsu, J. Ma, B.J. Morgan, M. Body, C. Legein, W. Dachraoui, M. Giannini, A. Demortière, M. Salanne, F. Dardoize, H. Groult, O.J. Borkiewicz, K.W. Chapman, P. Strasser, D. Dambournet, *Nat. Mater.* 16 (2017) 1142-1148.
- [29] Q. Gao, L. Yang, X. Lu, J. Mao, Y. Zhang, Y. Wu, Y. Tang, *J. Mater. Chem.* 20 (2010) 2807-2812.
- [30] Y. Xu, R. Wu, J. Zhang, Y. Shi, B. Zhang, *Chem. Commun.* 49 (2013) 6656-6658.
- [31] Y. Yu, J. Zhang, X. Wu, W. Zhao, B. Zhang, *Angew. Chem., Int. Ed.* 51 (2012) 897-900.
- [32] W. Bi, Z. Hu, X. Li, C. Wu, J. Wu, Y. Wu, Y. Xie, *Nano Res.* 8 (2015) 193-200.
- [33] M. Yang, J. Li, H. Li, L. Su, X. J. Wei, Z. Zhou, *Phys. Chem. Chem. Phys.* 14 (2012) 11048-11052.
- [34] W. Zhao, C. Zhang, F. Geng, S. Zhuo, B. Zhang, *ACS Nano* 8 (2014) 10909-10919.
- [35] T. Wang, G. Zhang, S. Ren, B. Jiang, *J. Alloys Compd.* 701 (2017) 1-8.
- [36] G.T. Kim, T.K. Park, H. Chung, Y.T. Kim, M.H. Kwon, J.G. Choi, *Appl. Surf. Sci.* 152 (1999) 35-43.
- [37] S. Vadahanambi, H. Park, *New J. Chem.* 42 (2018) 5668-5673.
- [38] C. Bommier, X. Ji, *Small* 14 (2018) 1703576.
- [39] A. Ponrouch, A.R. Goñi, M.R. Palacín, *Electrochem. Commun.* 27 (2013) 85-88.
- [40] Z. Le, F. Liu, P. Nie, X. Li, X. Liu, Z. Bian, G. Chen, H.B. Wu, Y. Lu, *ACS Nano* 11 (2017) 2952-2960.
- [41] Y. Wen, K. He, Y. Zhu, F. Han, Y. Xu, I. Matsuda, Y. Ishii, J. Cumings, C. Wang,

- Nat. Commun. 5 (2014) 4033.
- [42] R. Wang, S. Wang, X. Peng, Y. Zhang, D. Jin, P.K. Chu, L. Zhang, ACS Appl. Mater. Interfaces 9 (2017) 32745-32755.
- [43] A. Rudola, K. Saravanan, C.W. Mason, P. Balaya, J. Mater. Chem. A 1 (2013) 2653-2662.
- [44] X. Wang, S. Kajiyama, H. Iinuma, E. Hosono, S. Oro, I. Moriguchi, M. Okubo, A. Yamada, Nat. Commun. 6 (2015) 6544.
- [45] S. Tan, Y. Jiang, Q. Wei, Q. Huang, Y. Dai, F. Xiong, Q. Li, Q. An, X. Xu, Z. Zhu, Adv. Mater. 30 (2018) 1707122.
- [46] C. Zhao, C. Yu, M. Zhang, H. Huang, S. Li, X. Han, Z. Liu, J. Yang, W. Xiao, J. Liang, X. Sun, J. Qiu, Adv. Energy Mater. 7 (2017) 1602880.
- [47] X. Xia, D. Chao, Y. Zhang, J. Zhan, Y. Zhong, X. Wang, Y. Wang, Z.X. Shen, J. Tu, H.J. Fan, Small 12 (2016) 3048-3058.
- [48] D. Sheberla, J.C. Bachman, J.S. Elias, C.J. Sun, Y. Shao-Horn, M. Dincă, Nat. Mater. 16 (2017) 220.
- [49] Y. Xu, W. Cao, Y. Yin, J. Sheng, Q. An, Q. Wei, W. Yang, L. Mai, Nano Energy 55 (2019) 526-533.
- [50] R. Alcántara, M. Jaraba, P. Lavela, J.L. Tirado, Chem. Mater. 14 (2002) 2847-2848.
- [51] Q. Guo, Y. Ma, T. Chen, Q. Xia, M. Yang, H. Xia, Y. Yu, ACS Nano 11 (2017) 12658-12667.
- [52] J. Yue, Q. Sun, Z. Fu, Chem. Commun. 49 (2013) 5868-5870.
- [53] Q. Sun, Q.Q. Ren, H. Li, Z.W. Fu, Electrochem. Commun. 13 (2011) 1462-1464.

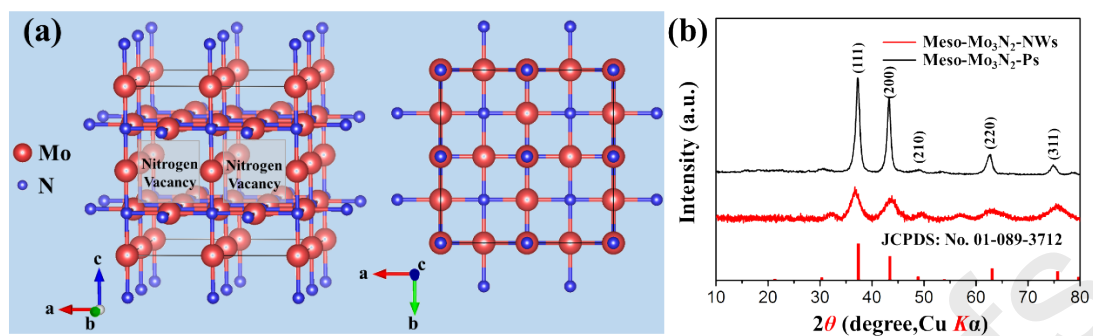


Fig. 1. (a) The cubic crystal structure of Mo_3N_2 with nitrogen vacancy; (b) XRD patterns of the Meso- Mo_3N_2 -Ps and Meso- Mo_3N_2 -NWs. The diffraction peaks of Meso- Mo_3N_2 -NWs exhibit the lower intensity and broad trend owing to the low calcination temperature.

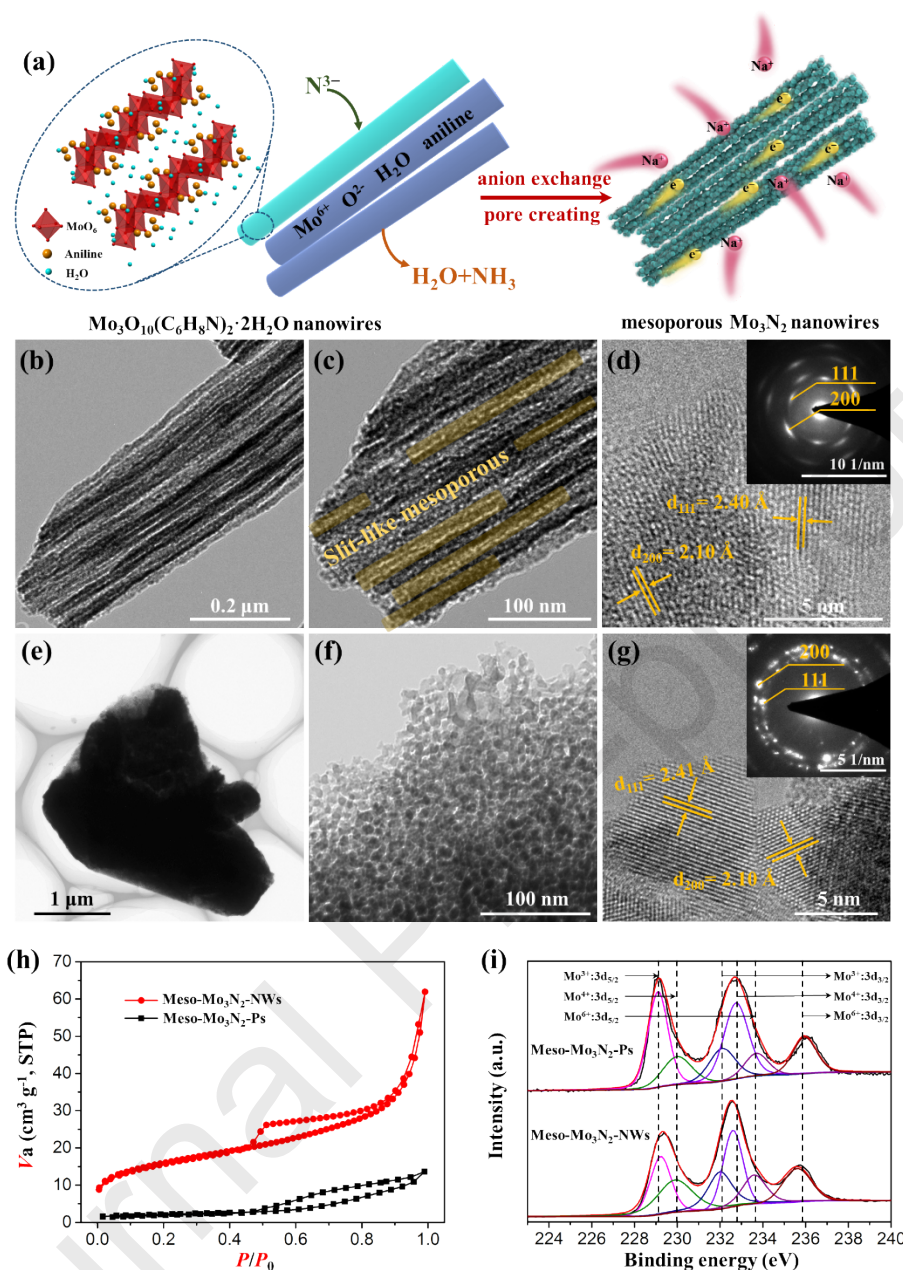


Fig. 2. Synthesis strategy, morphology characterizations and surface chemical composition characterizations of Meso- Mo_3N_2 -NWs and Meso- Mo_3N_2 -Ps. (a) Schematic of the transformation from $\text{Mo}_3\text{O}_{10}(\text{C}_6\text{H}_8\text{N})_2 \cdot 2\text{H}_2\text{O}$ nanowires to Meso- Mo_3N_2 -NWs, consisted of interconnected nanograins through the anion-exchange processes when annealing in ammonia atmosphere, providing effective electron&ion transport; TEM (b, c) and HRTEM (d) images of Meso- Mo_3N_2 -NWs; inset of (d) is the related SAED pattern; TEM (e, f) and HRTEM (g) images of Meso- Mo_3N_2 -Ps; inset of (g) is the related SAED pattern; nitrogen isotherm (h) and Mo 3d XPS spectra (i) of the Meso- Mo_3N_2 -NWs and Meso- Mo_3N_2 -Ps.

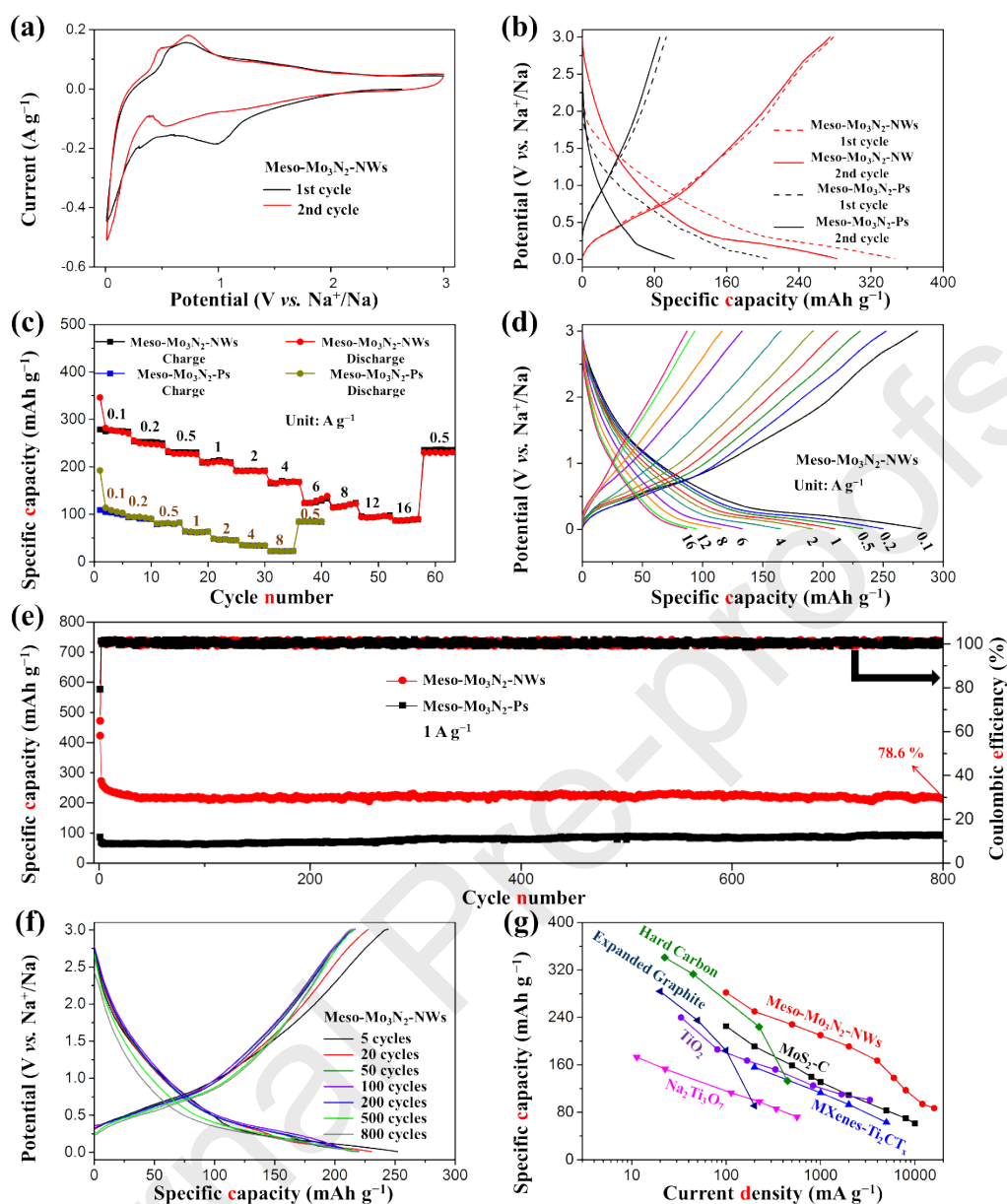


Fig. 3. Sodium-ion storage performance of Mo_3N_2 . (a) The first two cycles of CV curves at a sweep rate of 0.2 mV s^{-1} of the Meso- Mo_3N_2 -NWs; galvanostatic charge-discharge curves at 0.1 A g^{-1} (b) and rate performance at different specific currents ranging from 0.1 to 16 A g^{-1} (c) of Meso- Mo_3N_2 -NWs and Meso- Mo_3N_2 -Ps; (d) corresponding galvanostatic charge-discharge curves of Meso- Mo_3N_2 -NWs at different specific currents ranging from 0.1 to 16 A g^{-1} ; (e) long-term cycling performances at 1 A g^{-1} of Meso- Mo_3N_2 -NWs and Meso- Mo_3N_2 -Ps; (f) corresponding galvanostatic charge-discharge curves of Meso- Mo_3N_2 -NWs at different cycles at 1 A g^{-1} ; (g) rate capability for Meso- Mo_3N_2 -NWs compared to other anodes in reported literature: hard carbon [39], TiO_2 [40], expanded graphite [41], MoS_2 -C [42], $\text{Na}_2\text{Ti}_3\text{O}_7$ [43] and MXenes Ti_2CT_x [44].

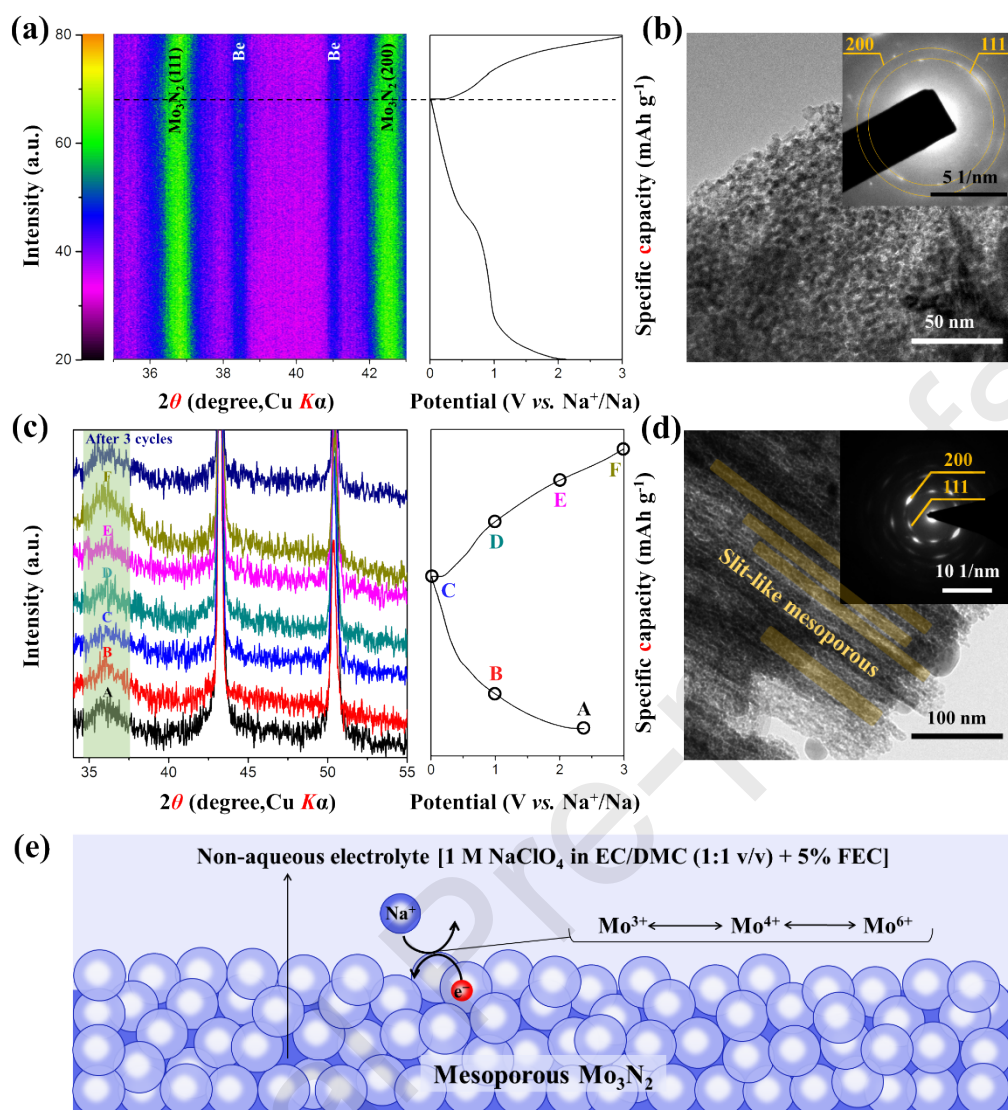


Fig. 4. Sodium-ion storage mechanism of Mo_3N_2 . *In-situ* XRD patterns of Meso- Mo_3N_2 -Ps (a), *ex-situ* XRD patterns of Meso- Mo_3N_2 -NWs (c) and corresponding galvanostatic charge-discharge curves at 0.1 A g^{-1} during the first cycle; TEM image of Meso- Mo_3N_2 -Ps (b) and Meso- Mo_3N_2 -NWs (d) when discharged to 0.01 V; inset of (b) and (d) are the related SAED patterns; (e) schematic of the sodium-ion storage mechanism for Mo_3N_2 .

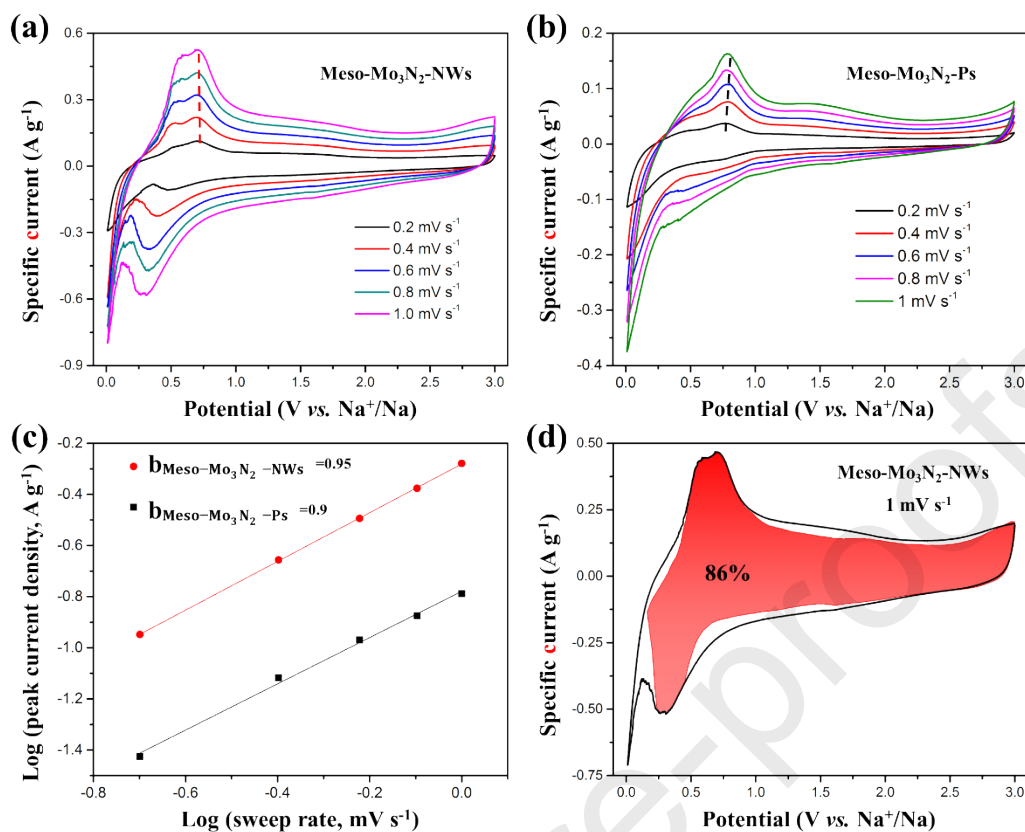
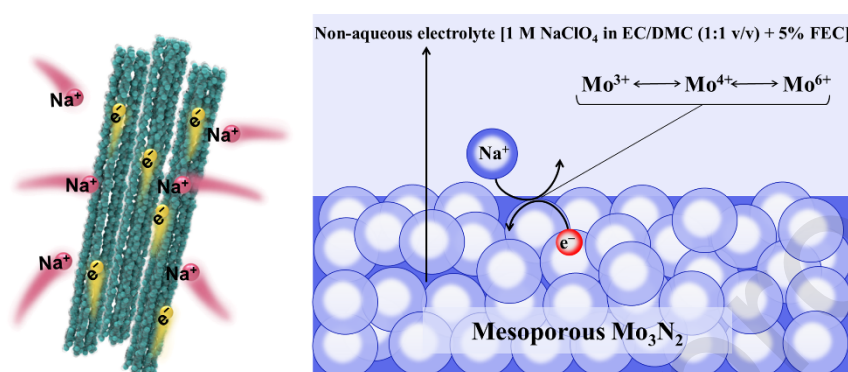


Fig. 5. CV curves of Meso-Mo₃N₂-NWs (a) and Meso-Mo₃N₂-Ps (b) at sweep rates ranging from 0.2 to 1 mV s⁻¹; (c) analysis of *b*-value of Meso-Mo₃N₂-NWs and Meso-Mo₃N₂-Ps by using the relationship between peak currents and scan rates; (d) CV curves of Meso-Mo₃N₂-NWs at 1 mV s⁻¹ with hatched portions for the capacitive contributions.

Graphical Abstract

The mesoporous Mo_3N_2 nanowires exhibit a capacitance-dominated sodium-ion storage process, which enables the high-rate capabilities. Besides, the sodium-ion storage mechanism of mesoporous Mo_3N_2 nanowires is surface redox reaction.



Declaration of interests

The authors declare that they have no known competing financial interests or personal relationships that could have appeared to influence the work reported in this paper.

The authors declare the following financial interests/personal relationships which may be considered as potential competing interests: